CHEMISTRY OF MATERIALS

ARTICLE

pubs.acs.org/cm

Novel Incipient Ferroelectrics Based on $Ba_4MNb_xTa_{10-x}O_{30}$ where M = Zn, Mg, Co, Ni

L. Wang,[†,‡] Y. Sakka,[†,‡] D. A. Rusakov,[§] Y. Mozharivskyj,[⊥] and T. Kolodiazhnyi*[,§]

[†]Graduate School of Pure and Applied Sciences, University of Tsukuba, 1-1-1 Tenodai, Tsukuba, Ibaraki 305-8571, Japan

[‡]National Institute for Materials Science, 1-2-1 Sengen, Tsukuba, Ibaraki, 305-0047, Japan

[§]National Institute for Materials Science, 1-1 Namiki, Tsukuba, Ibaraki, 305-0044, Japan

[⊥]Department of Chemistry, McMaster University, 1280 Main Street West, Hamilton, Ontario, Canada L8S 4M1

ABSTRACT: We report on structural, dielectric, magnetic and Raman data of the title compounds. Analysis of the single crystal diffraction data reveals that the ground state of the title compounds can be characterized within the *Cm* space group. The $Ba_4MTa_{10}O_{30}$ compounds show typical features of incipient ferroelectrics, i.e., their dielectric constant gradually increases on cooling and levels off or slightly decreases below 10 K. Nb solubility limit, *x*, for $Ba_4MNb_xTa_{10-x}O_{30}$ compositions equilibrated at 1450−1600 °C was determined by powder XRD and by electron probe microanalysis. Substitution of Nb for Ta leads to the low-temperature dielectric anomaly having a relaxor-type signature. The Co- and Ni-based compounds show paramagnetic behavior in the 2−300 K range with no indication of the magnetic long-range order.

KEYWORDS: incipient ferroelectrics, paramagnetism, dielectric loss

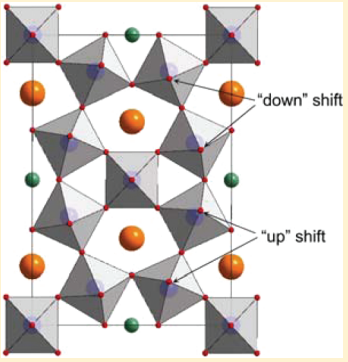

1. INTRODUCTION

Rare earth (RE) oxides are used extensively in the microwave and wireless communications. For example, gadolinium and dysprosium provide low insertion loss in the high-power microwave circulators and isolators based on the yttrium−gadolinium garnets.[1−3] Samarium, lanthanum, and neodymium are the major components of the microwave dielectric resonators utilized in the wireless base-stations, filters and satellite multiplexers.[4] Recent shortages in the RE supply have prompted wireless communication industry to look for an alternative, i.e., RE-free materials that can deliver similar performance.

Motivated by this challenge we undertook an exploratory study of several pseudoternary phases in the $BaO-MO-Ta_2O_5$ composition field, herein M stands for Mg, Co, Ni, and Zn. Our choice of these compositions was based upon two major reasons. First, several $BaO-MO-Ta_2O_5$ pseudoternary compounds, e.g., $Ba_9M(Ta,Nb)_{14}O_{45}$, are isostructural with the tetragonal tungsten bronze (TTB) $Ba_{6-3x}Sm_{8+2x}Ti_{18}O_{54}$ materials—a major component of coaxial microwave filters and duplexers.[5−8] Second, it is also known that several $BaO-MO-(Ta,Nb)_2O_5$ compounds show extremely low dielectric loss—an important property for microwave applications.[9,10]

A number of phases have been reported in the $BaO-MO-(Ta,Nb)_2O_5$ composition field.[11] Among those, the most technologically important are ordered perovskites based on $Ba_3MgTa_2O_9$, $Ba_3ZnTa_2O_9$ and $Ba_3CoNb_2O_9-Ba_3ZnNb_2O_9$ solid solutions.[12] These are widely used for ceramic dielectric resonators, microwave filters and multiplexers for wireless communication. Other ternary compounds in the Ba-rich part of the $BaO-MO-(Ta,Nb)_2O_5$ phase diagram include layered hexagonal perovskites,[12−15] e.g., $Ba_8ZnTa_6O_{24}$, $Ba_8CoNb_6O_{24}$, $Ba_{10}Mg_{0.25}Ta_{7.9}O_{30}$, and TTB-type phases, e.g., $Ba_9M(Ta,Nb)_{14}O_{45}$.[6,8,16] Structural and physical properties of these phases are well documented in the literature.[11,17] In particular, the ordered cubic perovskites and layered hexagonal perovskites show a modest dielectric constant and low dielectric loss, tan δ, as opposed to the TTB-type compounds that exhibit significantly higher dielectric loss together with large and temperature dependent dielectric constant typical for relaxor-type ferroelectrics.

In this paper we focus on the $Ba_4MTa_{10}O_{30}$ phases that form along the tie line between MTa_2O_6 and $BaTa_2O_6$ in the Ta-rich part of the $BaO-MO-Ta_2O_5$ phase diagram[18−21] These phases do not belong to the TTB-type compounds albeit they possess some common structural motifs. Early works on structural analysis of the $Ba_4MTa_{10}O_{30}$ phases with M = Mg, Co, Ni, Mn and Fe reported in refs 18−20 have assigned them to the noncentrosymmetric *Amm*2 space group. Recent work on the $BaO-ZnO-Ta_2O_5$ phase diagram could not confirm the existence of the $Ba_4ZnTa_{10}O_{30}$ compound.[21] Instead, a $Ba_3ZnTa_8O_{24}$ phase has been found along the $MTa_2O_6-BaTa_2O_6$ tie line.[21] Here we demonstrate that the $Ba_3ZnTa_8O_{24}$ phase is isotypical with the $Ba_4MTa_{10}O_{30}$ phases and discuss the reasons for the difference in the chemical composition of these phases. Dielectric properties of the $Ba_4MTa_{10}O_{30}$ phases are largely unknown. Recently Kolodiazhnyi et al., showed that the magnitude of the dielectric constant of $Ba_4MgTa_{10}O_{30}$ ceramics is similar to that of the $Ba_{6-3x}Sm_{8+2x}Ti_{18}O_{54}$ TTB-type

Received: January 14, 2011
Revised: March 28, 2011
Published: April 18, 2011

dx.doi.org/10.1021/cm200117y | *Chem. Mater.* 2011, 23, 2586–2594

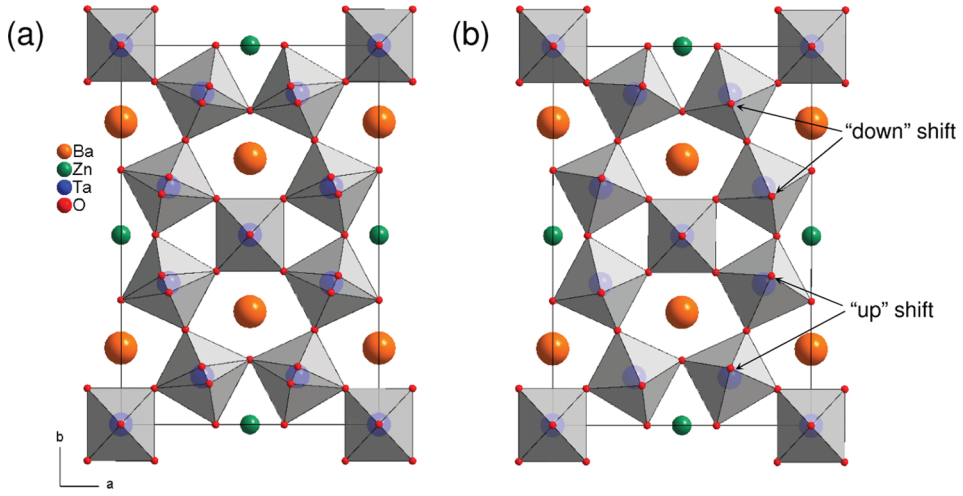

Figure 1. Crystal structure of the prototype $Ba_4ZnTa_{10}O_{30}$ compound refined in (a) *Cmmm* space group and, (b) *Cm* space group both viewed along the *c* axis. Only half of the Zn(2) positions are occupied.

materials.[11] In view of relatively large dielectric constant, it was conjectured that the $Ba_4MTa_{10}O_{30}$ compounds may belong to ferroelectric or incipient ferroelectric family. In this contribution we present a comprehensive analysis of the structural, dielectric, magnetic and Raman properties of the $Ba_4MTa_{10}O_{30}$ phases. Our single crystal analysis indicates that, in contrast to the early data,[18−20] all the samples studied can be assigned to the centrosymmetric *Cmmm* space group in better agreement with their dielectric properties. We find that the Ta-based materials demonstrate incipient ferroelectric properties in the 3−300 K range. Partial substitution of Nb for Ta causes a distinct low-temperature anomaly with a frequency dispersive dielectric constant. On the basis of the detailed structural analysis, we find that the random tilting of the oxygen octahedra associated with the partially occupied M-sites is responsible for the relaxor-type behavior as well as for relatively high dielectric loss in these materials.

2. EXPERIMENTAL SECTION

Samples were prepared from 99.99% pure $BaCO_3$, Co_3O_4, MgO, NiO, Ta_2O_5, and Nb_2O_5. The stoichiometric mixtures were treated at 1200−1300 °C for 20 h, with intermediate regrinding. Dense ceramic bodies were obtained by sintering in air at 1400−1600 °C for 10−20 h. Phase purity was confirmed by powder X-ray diffraction (Rigaku Ultima III X-ray diffractometer with Cu K_α X-ray source). Lattice parameters were obtained from Rietveld refinement of the X-ray data using RIETAN 2000. During the course of the studies it was noticed that substitution of Nb for Ta resulted in ceramics with large crystallite size of ca. 1000 μm. Small single crystals were extracted from the crashed ceramics and subjected to the single crystal analysis. Magnetic susceptibility in the 2−300 K range was measured using superconducting quantum interference devise (MPMS, Quantum Design). For dielectric measurements, Au electrodes were spattered on the disk-shaped ceramic samples of 6 mm diameter and 1 mm thick. Dielectric properties in the 20 Hz to 2 MHz frequency range were measured with Agilent E4980 Precision LCR Meter in the temperature interval of 3−300 K. For temperature measurements of the dielectric properties, a homemade dielectric cell coupled with commercial cryostat (PPMS, Quantum Design) has been used.[22] Room-temperature Raman spectra (Jobin Yvon/Horiba) on the fine-polished sample surface were measured in the backscattered geometry in the 20 cm^{-1} to 900 cm^{-1} frequency range. Quantitative elemental composition of the samples was determined by electron probe microanalysis (EPMA) using wavelength-dispersive (WDS) X-ray spectroscopy (model JXA-8500F, JEOL). The EPMA analysis was performed on polished surfaces of selected samples by averaging the data taken from 5 to 6 locations of selected grain.

Table 1. Crystallographic Data and Refinement Results for the $Ba_3ZnNbTa_7O_{24}$ Single Crystals

T	293 K	100 K
refined composition	$Ba_{3.56(3)}Zn_{1.44(3)}$ $Nb_{0.89}Ta_{9.11}O_{30}$	$Ba_{3.51(2)}Zn_{1.49(2)}$ $Nb_{0.89}Ta_{9.11}O_{30}$
space group	*Cmmm*	*Cm*
unit-cell dimensions (Å)	a = 10.2115(3)	a = 10.2092(2)
	b = 14.9714(4)	b = 14.9406(3)
	c = 3.8950(1)	c = 3.8938(1)
		β = 90.016(6)°
V (Å^3)	595.47(3)	593.93(2)
Z	1	1
Θ range	2.41−44.89°	2.42−45.84°
GOF on F^2	1.006	1.020
final R indices	R_1 = 0.0421,	R_1 = 0.0404,
$[I > 2\sigma(I)]$	wR_2 = 0.0863	wR_2 = 0.0856
R indices (all data)	R_1 = 0.0590,	R_1 = 0.0546,
	wR_2 = 0.0935	wR_2 = 0.0936
largest peak and hole (e$^-$/Å^3)	4.440/−6.731	4.596/−4.377

3. RESULTS AND DISCUSSION

A. Single-Crystal X-ray Analysis. A single crystal was extracted from the annealed $Ba_3ZnNbTa_7O_{24}$ sample and mounted on the tip of the glass fiber. Room-temperature (293 K) and low-temperature (100 K) data were collected on a Bruker Apex II diffractometers with Mo K_α radiation. The data were collected until 2Θ = 90° in order to obtain precise positional and vibrational parameters for the oxygen atoms. A numerical absorption correction was based on the crystal shape derived from optical face indexing. Structural determination and refinement were performed using the SHELXL package.[23]

Analysis both of the room- and low-temperature reflections indicated a *C*-centered cell without glide planes, and an

dx.doi.org/10.1021/cm200117y |*Chem. Mater.* 2011, 23, 2586–2594

Table 2. Atomic and Equivalent Isotropic Temperature (U) Parameters of the $Ba_3ZnNbTa_7O_{24}$ Single Crystal for the *Cmmm* (293 K) and *Cm* (100 K) Solutions

atom	site	occupancy	x	y	z	U (Å^2)
			Cmmm (293 K)			
Ba/Zn(1)	4*j*	0.890/0.110(8)	0	0.20190(6)	1/2	0.0149(2)
Zn(2)	2*c*	0.5	1/2	0	1/2	0.0116(6)
Ta/Nb(3)	2*a*	0.911/0.089	0	0	0	0.0066(1)
Ta/Nb(4)	8*p*	0.911/0.089	0.31534(3)	0.87315(3)	0	0.0079(1)
O(1)	8*p*	1	0.1300(5)	0.0954(5)	0	0.015(1)
O(2)	8*m*	0.5	1/4	1/4	0.0987(30)	0.011(2)
O(3)	8*q*	0.5	0.3421(18)	0.8926(12)	1/2	0.021(2)
O(4)	8*q*	0.5	0.3134(16)	0.8476(12)	1/2	0.021(2)
O(5)	4*i*	1	0	0.3286(6)	0	0.010(1)
O(6)	8*o*	0.5	0.3671(10)	0	0.0974(34)	0.014(2)
O(7)	2*d*	1	0	0	1/2	0.019(3)
			Cm (100 K)			
Ba/Zn(1)	4*b*	0.878/0.122(6)	0	0.20168(3)	1/2	0.0092(1)
Zn(2)	2*a*	0.5	1/2	0	1/2	0.0060(3)
Ta/Nb(3)	2*a*	0.911/0.089	0	0	0	0.0036(1)
Ta/Nb(4)	4*b*	0.911/0.089	0.31554(2)	0.87300(1)	0	0.0049(2)
Ta/Nb(5)	4*b*	0.911/0.089	0.68446(2)	0.87301(1)	0	0.0051(2)
O(1)	4*b*	1	0.1302(2)	0.0961(2)	0	0.0103(6)
O(1A)	4*b*	1	0.8698(2)	0.9039(2)	0	0.0103(6)
O(2)	4*b*	1	1/4	1/4	0.0984(17)	0.0078(9)
O(3)	4*b*	1	0.3454(11)	0.8950(7)	1/2	0.022(2)
O(4)	4*b*	1	0.68787(7)	0.8488(5)	1/2	0.008(1)
O(5)	4*b*	1	0	0.3279(3)	0	0.0077(9)
O(6)	2*a*	1	0.6344(7)	0	0.0953(24)	0.014(1)
O(6A)	2*a*	1	0.3656(7)	0	0.0953(24)	0.014(2)
O(7)	2*a*	1	0	0	1/2	0.019(2)

unrestricted refinement of the unit cell parameters (i.e., within the triclinic symmetry) yielded the α, β, and γ angles to be 90° within 3 standard deviations, σ. Thus, the original structural solution proceeded with the orthorhombic symmetry. Both noncentrosymmetric (*Cmm*2, *C*222, and *Amm*2) and centrosymmetric (*Cmmm*) space groups were tested. Irrespectively of the space group, some of the oxygen sites had to be split and half occupied to account for significant residual densities. The residual electron density was more pronounced for the low-temperature data. Out of the tested, only the *Cmmm* space group provided a stable refinement (Figure 1, Table 1 and 2) without correlations between the atomic parameters and with positively defined anisotropic temperature factors for all oxygen atoms. To prove that the refinement results were independent of the crystal quality, we picked up and tested another crystal. The refined positional and vibrational parameters were similar.

Presence of the split and half-occupied sites could be indicative of the existence of a superstructure or lower symmetry. The reciprocal space generated from the room- and low-temperature data revealed no superstructure reflections. In view of these results, we proceeded with a lower symmetry and used a bottom-up approach to establish the correct structure. The original structural solution was based on the room-temperature data, but the same results were obtained later for the low-temperature data. The structure was solved in the *P*1 space group, which eliminates any symmetry constrains on the atomic positions. The analysis of the obtained model revealed that a mirror plane, perpendicular to b_{orth}, is present, and thus the correct symmetry is *Cm* as shown in Figure 1b. At this stage, it became also obvious that the lower symmetry stems from the positions of some oxygen sites, primarily O3 and O4, while the positions of the metal sites obey the higher *Cmmm* symmetry (the origin of the symmetry lowering is discussed later). Unit-cell refinements against observed reflections indicated that the unit cell is metrically orthorhombic (β = 90.016(6)° for the 100 K data). During the refinement in the *Cm* space group, the positional parameters of the Ta/Nb4 and Ta/Nb5 sites were related within 3σ as x(Ta/Nb5) = 1 − x(Ta/Nb4), y(Ta/Nb5) = y(Ta/Nb4), and z(Ta/Nb5) = z(Ta/Nb4) = 0. These relationships represent the underlying *Cmmm* symmetry, within which these two sites are combined into one Ta/Nb4 site (Table 2). Also, the underlying higher *Cmmm* symmetry was also detected for the Ba/Zn1, Zn, O1/O1A, O5, and O7 sites, whereas the O2 and O6/O6A sites could be described within the *Cmm*2 one. Although for some sites, correlations between the positional parameters similar to those between Ta/Nb4 and Ta/Nb5 were observed, in other cases the positional parameters were close to 0, 1/4, and 1/2 within 3σ, which is indicative of higher symmetries. Introducing restrains for such sites reduced the atomic correlations and provided a more stable refinement in the *Cm* space group. It has to be emphasized that the O3 and O4 positions could be described

Table 3. Chemical Composition Based on EPMA WDS Microanalysis of Ceramic Grains for Selected $Ba_4MNb_xTa_{10-x}O_{30}$ samples

target composition	Ba (at %)	M (at %)	Nb (at %)	Ta (at %)
$Ba_3ZnNbTa_7O_{24}$	10.075 ± 0.048	Zn = 2.679 ± 0.058	2.25 ± 0.030	22.98 ± 0.22
$Ba_4MgNb_2Ta_8O_{30}$	10.497 ± 0.047	Mg = 2.812 ± 0.030	4.801 ± 0.038	20.670 ± 0.095
$Ba_4CoNb_4Ta_6O_{30}$	10.633 ± 0.046	Co = 2.466 ± 0.027	9.942 ± 0.090	15.630 ± 0.083

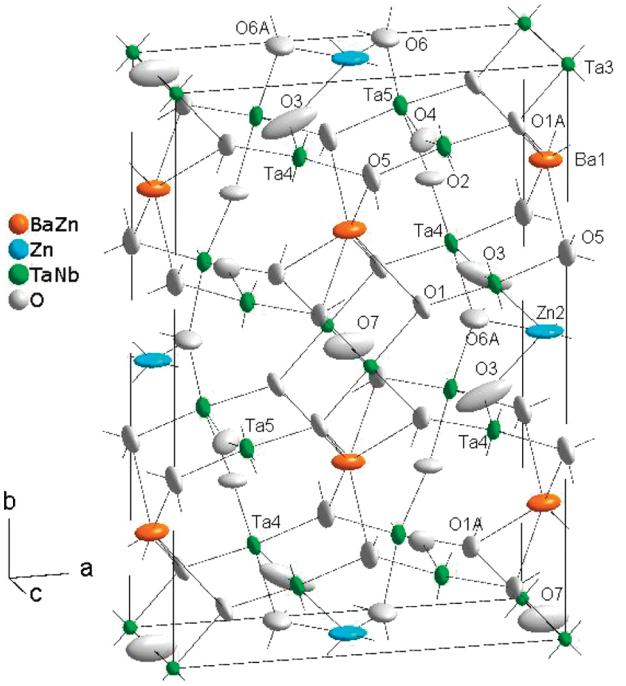

Figure 2. Schematic diagram of the $Ba_3ZnNbTa_7O_{24}$ crystal structure that shows thermal atomic displacement ellipsoids.

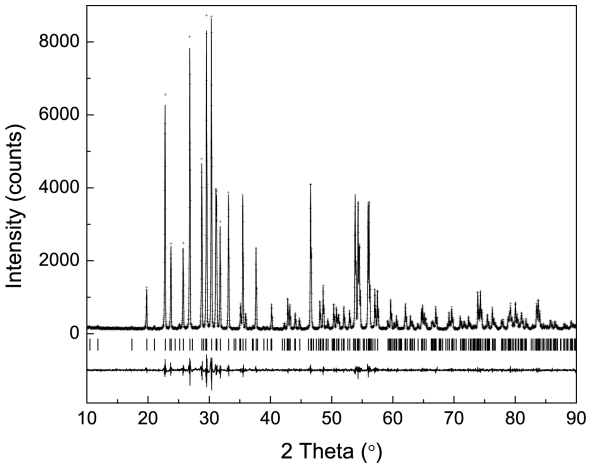

Figure 3. Room-temperature X-ray diffraction pattern of $Ba_3ZnNbTa_7O_{24}$ (+). Calculated diffraction pattern from Rietveld refinement (solid line) with GOF = 1.29, R_P = 5.08% and R_{WP} = 6.79%. The vertical bars indicate the positions of expected Bragg peaks. The difference between observed and calculated data is shown at the bottom of the plot.

only within the *Cm* space group and thus no restrains were applied to these sites. Anisotropic temperature factors for all O atoms were refined and they were positively defined.

Other points, which have to be addressed during the refinement, are Ba/Zn and Nb/Ta mixing and Zn deficiency. The O sites could not be used as an "electron density reference" to refine reliably of the mixing/occupation parameters for the metal sites, as the oxygen is the lightest element in the system. Instead we used the quantitative EPMA results and fixed the Ta/Nb ratio at 0.911/0.089 in agreement with the EPMA WDS analysis (Table 3). The same ratio was assumed for all Ta/Nb sites, as refining the Ta/Nb mixing when the Ba/Zn content was fixed yielded identical occupancies within 3σ for all Ta/Nb sites both in *Cm* and *Cmmm*. During the refinement, the Zn occupancy on the Zn2 site was 50% within 3σ and, thus, was fixed at 50% during the final stages of the refinement both in *Cm* and *Cmmm*. The refinement results for the room- and low-temperature data within individual symmetries were similar, however the O positions are better defined from the 100 K data, specifically within the *Cm* model. Besides, the refinement of the 100K data in the *Cmmm* model produced much higher residual electron densities when compared to the room-temperature results with the same symmetry. Thus, while the room-temperature structure may be represented by the *Cmmm* model, the low-temperature one is better described by the *Cm* model. Table 1 and 2 provides crystallographic data and refinement results for the two models at the two temperatures.

The *Cmmm* structural model (Figure 1) of $Ba_3ZnNbTa_7O_{24}$ is similar to the structure of $K_2YNb_5O_{15-\delta}$ ($K_4Y_2Nb_{10}O_{30-\delta}$),[24] except that in $K_2YNb_5O_{15-\delta}$, the Y site is fully occupied and in $Ba_3ZnNbTa_7O_{24}$ the corresponding Zn site is half occupied to keep the charge balance. Another distinction between these *Cmmm* structures is a disordered nature of the oxygen atoms that form octahedra around the Ta/Nb4 site in $Ba_3ZnNbTa_7O_{24}$. These oxygen atoms form disordered $(Ta/Nb)O_6$ octahedra, but within the *Cmmm* model, the distortion appears to be random.

The nature of the distortion becomes clear in the *Cm* model, specifically from the 100 K data (Figure 1b). The corner-sharing $(Ta/Nb4/5)O_6$ octahedra running along the *b* direction exhibit significant distortions which can be described as "up" or "down" concomitant shifts of the apical O3 and O4 atoms. Within each octahedral chain, two "up" O shifts are followed by two "down" ones, but between the chains the distortion sequence is displaced by *b*/2. These O3 and O4 shifts are responsible for the observed *Cm* symmetry, as the positional parameters of the metal and O1/O1A, O5 and O7 sites are within three standard deviations from those of the *Cmmm* model. Besides, the correlations between the unrestrained Ta/Nb4 and Ta/Nb5, O1 and O1A positional parameters during the refinement were unusually large, which was also indicative of an underlying higher symmetry. Additionally, the restrains put on the O2 and O6/O6A sites obey the *Cmm*2 symmetry, which is a subgroup of the *Cmmm* symmetry. The *Cmmm* symmetry requires presence of the equivalent sites at $-z$ for O2 and O6/O6A but no significant residual electron density was detected at $-z$. Another interesting point is that the *z* coordinates

dx.doi.org/10.1021/cm200117y |*Chem. Mater.* 2011, 23, 2586–2594

Table 4. Lattice Parameters of the Studied Compounds Refined within the *Cmmm* Space Group

target composition	a (Å)	b (Å)	c (Å)	V (Å^3)
$Ba_4MgTa_{10}O_{30}$	10.2146(5)	14.9744(7)	3.89850(17)	596.31(8)
$Ba_4MgNbTa_9O_{30}$	10.2140(6)	14.9754(9)	3.9012(2)	596.72(11)
$Ba_4MgNb_2Ta_8O_{30}$	10.2124(6)	14.9791(9)	3.9033(2)	597.10(11)
$Ba_4CoTa_{10}O_{30}$	10.2027(8)	14.9766(11)	3.8989(3)	595.90(12)
$Ba_4CoNbTa_9O_{30}$	10.2001(5)	14.9739(7)	3.90007(19)	595.68(9)
$Ba_4CoNb_2Ta_8O_{30}$	10.1989(5)	14.9770(7)	3.90181(17)	596.00(8)
$Ba_4CoNb_4Ta_6O_{30}$	10.1946(4)	14.9837(6)	3.90658(15)	596.75(7)
$Ba_4NiTa_{10}O_{30}$	10.2166(4)	15.0877(6)	3.94703(16)	608.40(7)
$Ba_3ZnTa_8O_{24}$	10.1998(4)	14.9543(6)	3.8935(2)	593.87(7)
$Ba_3ZnNbTa_7O_{24}$	10.2057(3)	14.9592(4)	3.89499(10)	594.66(5)
$Ba_3ZnNb_2Ta_6O_{24}$	10.2008(5)	14.9596(8)	3.8955(2)	594.45(9)
$Ba_3ZnNb_3Ta_5O_{24}$	10.2014(3)	14.9713(4)	3.90071(11)	595.76(5)

for the O2 and O6/O6A are identical within 3σ. Although such a correlation can be considered a coincidence because these sites are not symmetry-related within any discussed structural model, such correlations may indicate that at higher temperature these sites may become special sites with $z = 0$.

Although the *Cm* model provides the best description of the atomic parameter at 100 K, the significant vibrational parameters of the O atoms suggest that distortions of the (Ta/Nb)O_6 octahedra may not have fully settled in. In particular, the O3 ellipsoids are highly elongated along the "shift" directions which likely represent additional octahedral tilting even at low-temperatures (Figure 2). It can be also speculated that at higher temperatures the co-operative tilting of the octahedra diminishes while tilting of the individual octahedra remains. In this case, the *Cmmm* model would provide a better structural description.

B. Powder X-ray Analysis and Refinement. For Rietveld refinement of the powder X-ray diffraction data we have used the structural model derived from the single-crystal X-ray analysis. Powder X-ray data were refined within the *Cmmm* space group using fractional atomic coordinates of the $Ba_3ZnNbTa_7O_{24}$ single crystal as initial parameters. The lattice parameters of the $Ba_4MTa_{10}O_{30}$ powder samples are given in Table 4. Figure 3 shows the observed, calculated and difference X-ray powder diffraction pattern of the $Ba_3ZnNbTa_7O_{24}$ as an example. Substantial solubility of Zn ions on Ba-sites, as revealed by the single-crystal $Ba_3ZnNbTa_7O_{24}$ data, provides a clue as to why the Zn-based compounds are formed closer to the MTa_2O_6 end member as compared to the rest of the $Ba_4MTa_{10}O_{30}$ phases studied.[18−20] As a result of the partial substitution of Zn for Ba, the chemical composition of $Ba_3ZnTa_8O_{24}$ compound can be reformulated as $(Ba_{3.75}Zn_{0.25})ZnTa_{10}O_{30}$. Therefore, the $Ba_3ZnTa_8O_{24}$ phase originally found by Roth et al.[21] is isostructural with the rest of the $Ba_4MTa_{10}O_{30}$ compounds reported in this work. The possible origin of the significant solubility of Zn on the Ba-site might be due to the larger ionic radius of Zn^{2+} as compared to Mg^{2+}, Co^{2+}, and Ni^{2+} ions.

Because of the similar ionic radii, most of the Ta^{5+} compounds also have their Nb^{5+} analogues. For example, both $Ba_9MTa_{14}O_{45}$ and $Ba_9MNb_{14}O_{45}$ end members of the TTB-type compounds are known.[6,8] In contrast, single-phase Nb-based analogues of the corresponding $Ba_4MTa_{10}O_{30}$ compounds do not exist. Several attempts to prepare the $Ba_4MNb_{10}O_{30}$ target compounds always resulted in the mixture of the MNb_2O_6 and $BaNb_2O_6$ pseudobinaries. Only partial substitution of Ta with

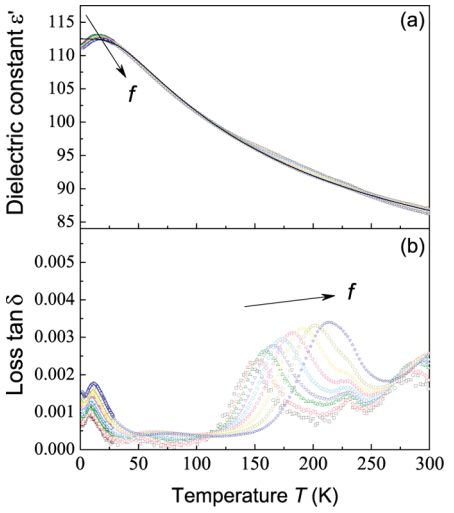

Figure 4. Temperature dependence of (a) dielectric constant, ε', and (b) dielectric loss, tan δ, of $Ba_4MgTa_{10}O_{30}$ at selected frequencies f = 0.5, 1, 2, 5, 10, 20, 50, 100, 200, and 500 kHz. Solid line which coincides with the ε' data points is a fit of $\varepsilon'(T)$ data to the Barrett equation. The fitting parameters are given in Table 5.

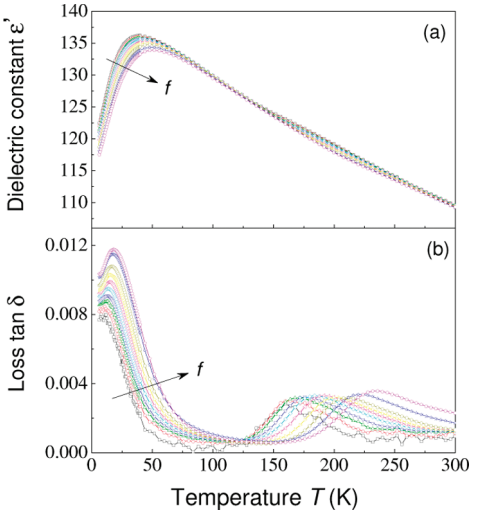

Figure 5. Temperature dependence of (a) dielectric constant, ε', and (b) dielectric loss, tan δ, of $Ba_4MgNb_2Ta_8O_{30}$ at selected frequencies f = 0.5, 1, 3, 6, 15, 34, 80, 185, 430, and 1000 kHz.

Nb has been achieved. It was found that $Ba_4CoNb_xTa_{10-x}O_{30}$ has the largest solubility of Nb with $x \leq 4$, whereas single-phase $Ba_4NiNb_xTa_{10-x}O_{30}$, forms only at $x < 1$. Single phases of $Ba_4MgNb_xTa_{10-x}O_{30}$ and $Ba_3ZnNb_xTa_{8-x}O_{24}$ were found for $x \leq 2$ and $x \leq 3$, respectively. The unit cell volume of $Ba_4MNb_xTa_{10-x}O_{30}$ shows a tendency to increase with Nb substitution (Table 4). The partial incorporation of Nb for Ta in the studied compounds has been also confirmed by the EPMA analysis. The reason for the limited substitution of Nb for Ta is not entirely clear and may require further studies that are beyond the scope of the present paper.

C. Dielectric Properties. Temperature dependence of the dielectric constant and dielectric loss of selected samples measured at various frequencies are shown in Figures 4−9. The room-temperature dielectric constants fall in the range of

dx.doi.org/10.1021/cm200117y |*Chem. Mater.* 2011, 23, 2586–2594

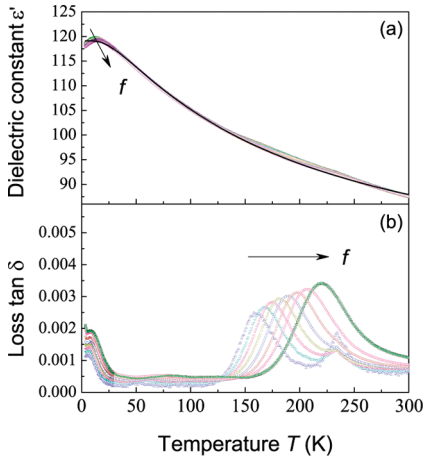

Figure 6. Temperature dependence of (a) dielectric constant, ε', and (b) dielectric loss, tan δ, of $Ba_4CoTa_{10}O_{30}$ at selected frequencies f = 0.5, 1, 2, 5, 10, 20, 50, 100, 200, and 500 kHz. Solid line that coincides with the ε' data points is a fit of $\varepsilon'(T)$ data to the Barrett equation. The fitting parameters are given in Table 5.

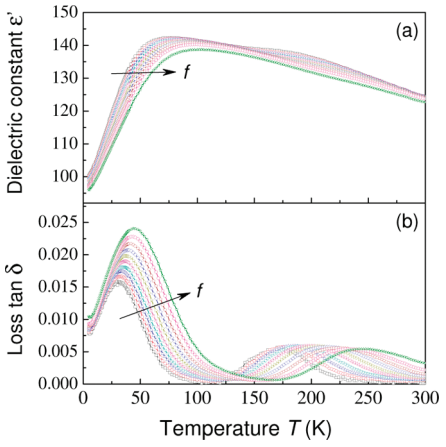

Figure 7. Temperature dependence of (a) dielectric constant, ε', and (b) dielectric loss, tan δ, of $Ba_4CoNb_4Ta_6O_{30}$ at selected frequencies f = 0.5, 1, 3, 6, 15, 34, 80, 185, 430, and 1000 kHz.

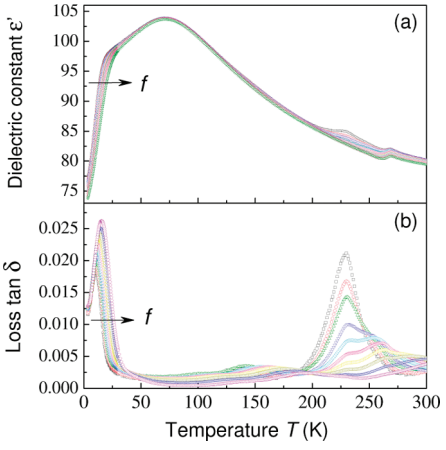

Figure 8. Temperature dependence of (a) dielectric constant, ε', and (b) dielectric loss, tan δ, of $Ba_4NiTa_{10}O_{30}$ at selected frequencies f = 0.5, 1.1, 2.7, 6.3, 14.6, 34.1, 79.3, 184.6, 430, and 1000 kHz.

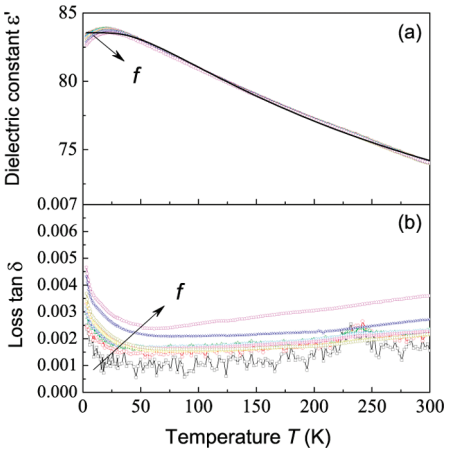

Figure 9. Temperature dependence of (a) dielectric constant, ε', and (b) dielectric loss, tan δ, of $Ba_3ZnNbTa_7O_{24}$ at selected frequencies f = 0.5, 1, 3, 6, 15, 34, 80, 185, 430, and 1000 kHz. Solid line is a fit of $\varepsilon'(T)$ data to the Barrett equation. The fitting parameters are given in Table 5.

Table 5. Parameters of the Fit to the Barrett Equation for Selected Incipient Ferroelectric Compounds

composition	A	C ($\times 10^4$ K)	T_0 (K)	T_1 (K)	ref
$Ba_4MgTa_{10}O_{30}$	70.4	6.63	−102.5	110.0	this work
$Ba_4CoTa_{10}O_{30}$	65.6	10.0	−147.9	78.2	this work
$Ba_3ZnTa_8O_{24}$	54.9	9.46	−300	100	this work
$Ba_3ZnNbTa_7O_{24}$	59.0	9.2	−300	150.3	this work
$CaTiO_3$	43.9	4.77	−111	110	26
$KTaO_3$	47.5	5.45	13.1	56.9	29
c-axis TiO_2	81.7	3.95	−165	135.4	30

70−140. Upon decrease in temperature, the $Ba_4MgTa_{10}O_{30}$, $Ba_4CoTa_{10}O_{30}$ and $Ba_3ZnTa_8O_{24}$ samples exhibit an increase in the ε' by ca. 20−30%. At temperature below 20 K, ε' reaches saturation and even slightly decreases. This $\varepsilon'(T)$ behavior is common for incipient ferroelectrics, where the low-temperature quantum fluctuations prevent "condensation" of the ferroelectric phase.[25,26] In the first approximation, the temperature dependence of dielectric constant of incipient ferroelectric is given by the Barrett equation[25]

$$\varepsilon = A + C\left(\frac{T_1}{2}\coth\frac{T_1}{2T} - T_0\right)^{-1} \quad (1)$$

where T_0 is the hypothetical Curie Temperature and T_1 is the onset temperature of quantum fluctuations. The parameters of the fit of the dielectric data of selected compounds to the eq 1 are given in Table 5 together with the data for other well-known incipient ferroelectrics. Most of the studied compounds demonstrate rather low T_0 values indicating that the paraelectric phase here is quite sable in contrast to $SrTiO_3$ and $KTaO_3$ compounds that are much closer to the limit of the paraelectric phase stability.

$Ba_4NiTa_{10}O_{30}$, on the other hand, appears an exception to the studied compounds and shows pronounced drop in ε' below 25 K accompanied by a sharp peak in dielectric loss that indicates a more complex dielectric behavior with a possibility of the low-temperature phase transition (Figure 8). In addition to the low-T drop in ε', $Ba_4NiTa_{10}O_{30}$ also shows another anomaly both in ε' and tan δ at around 260 K. This distinct dielectric

dx.doi.org/10.1021/cm200117y |Chem. Mater. 2011, 23, 2586–2594

Table 6. Room-Temperature ε', tan δ at 100 kHz, τ_ε as Well As Debye Relaxation Parameters of Selected Compounds

composition	ε'	tan δ	τ_ε ($\times 10^{-6}$K^{-1})	f_1 (Hz)	E_1 (meV)	f_2 (Hz)	E_2 (meV)
$Ba_4MgTa_{10}O_{30}$	91	0.00300	−765	2.16×10^{11}	13.4	2.59×10^{12}	284
$Ba_4MgNb_2Ta_8O_{30}$	105	0.00114	−787	2.26×10^{12}	86.7	8.17×10^{13}	349
$Ba_4CoTa_{10}O_{30}$	86	0.00980	−804	1.28×10^{12}	13.9	2.32×10^{14}	288
$Ba_4CoNb_4Ta_6O_{30}$	134	0.00194	−872	2.58×10^{13}	67.1	3.65×10^{14}	412
$Ba_4NiTa_{10}O_{30}$	80	0.04449	−597	6.91×10^{11}	19.0	1.65×10^{12}	251
$Ba_3ZnTa_8O_{24}$	66	0.00538	−328				
$Ba_3ZnNbTa_7O_{24}$	70	0.00098	−419				

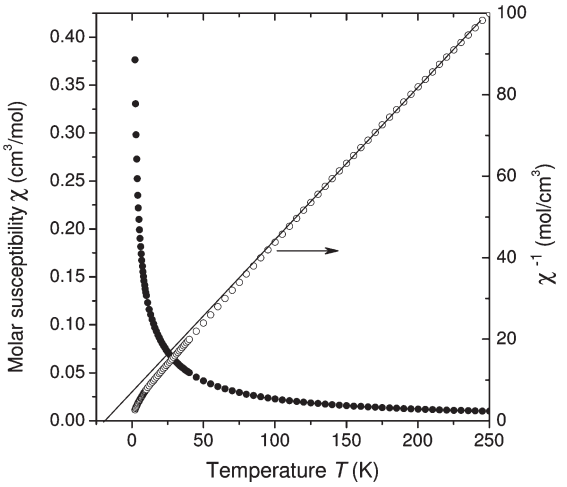

Figure 10. Temperature dependence of molar magnetic susceptibility of $Ba_4CoTa_{10}O_{30}$.

behavior most likely originates from the noticeably larger unit-cell volume of the $Ba_4NiTa_{10}O_{30}$ as compared to the rest of the phases listed in Table 4.

It is well-known that structural defects and impurities act as nucleation centers that can induce ferroelectric phase or polar nanoregions in the quantum paraelectric host. Typical examples of this behavior include Ca, Ba, and Pb-doped $SrTiO_3$ as well as Nb-, Li-, and Mn-doped $KTaO_3$.[27,28,31,32] It might be expected, therefore, that partial substitution of Nb for Ta in the title compounds may bring about a low-temperature phase transition to a lower symmetry phase or, at least, a dipolar glass behavior. Dielectric properties of selected compounds with partial Nb substitution that show a clear dielectric anomaly at low temperatures are shown in Figures 5 and 7. Strong frequency dependence of the ε' and dielectric loss maxima indicates the relaxor nature of this anomaly that resembles dipolar glass behavior observed in Li-doped $KTaO_3$.[33]

Except for $Ba_3ZnTa_{8-x}Nb_xO_{24}$ (e.g., Figure 9) that shows dispersion-less behavior, the dielectric constant of the rest of the compounds shows at least two dispersion regions at the low ($T \leq 90$ K) and high ($T \geq 150$ K) temperature regions. The Debye relaxation frequency (f_1 and f_2) and activation energy (E_1 and E_2) of the low- and high-temperature dielectric dispersion were estimated from the frequency dependence of the temperature of the tan δ maximum, T_{max}, according to

$$f = f_i \exp\left(-\frac{E_i}{k_B T_{max}}\right) \quad (2)$$

Table 7. Fitting Parameters for Magnetic Susceptibility of $Ba_4CoTa_{10}O_{30}$ and $Ba_4NiTa_{10}O_{30}$

composition	Θ_W (K)	p (μ_B)
$Ba_4CoTa_{10}O_{30}$	−11.4	1.45
$Ba_4NiTa_{10}O_{30}$	−36.2	0.723

where f_i is the characteristic Debye relaxation frequency, E_i is the activation energy, k_B is the Boltzmann constant. The f_i and E_i data obtained from eq 2 are summarized in Table 6. The table also shows room temperature dielectric constant, ε, its temperature coefficient, τ_ε, and tan δ measured at 100 kHz.

From the point of view of practical applications, the title compounds possess high dielectric constant. These materials might potentially replace dielectric resonators based on the rare-earth TTB-type $Ba_{6-3x}Sm_{8+2x}Ti_{18}O_{54}$ with $\varepsilon' \approx 70-90$ that are currently used in the 0.9−2.5 GHz microwave frequency range.[4,34] However, to be competitive with the latter materials, the title compounds have to be optimized with respect to the dielectric loss, tan δ, and τ_ε, both of which are still too high for practical applications. One of the possible solution is to alloy the title compounds with the *Cmmm*-type $K_4Y_2Nb_{10}O_{30}$. This should relax the distortions of the oxygen octahedra and reduce the anharmonic component in the lattice vibrations, which could be beneficial for reduction of the dielectric loss and τ_ε.

D. Magnetic Properties. Among the title compounds, $Ba_4CoTa_{10}O_{30}$ and $Ba_4NiTa_{10}O_{30}$ contain magnetically active d^7 Co^{2+} and d^8 Ni^{2+} ions in the $S = 3/2$ and $S = 1$ spin ground state, respectively. To investigate possible magnetic interactions of these ions we measured temperature dependence of magnetic susceptibility, χ, in the 2−300 K range. An example of the temperature dependence of χ measured at $H = 200$ Oe is shown for $Ba_4CoTa_{10}O_{30}$ in Figure 10. We found no indication of the long-range magnetic ordering in both $Ba_4CoTa_{10}O_{30}$ and $Ba_4NiTa_{10}O_{30}$ down to the lowest measured temperature of 2 K. The absence of the long-range magnetic ordering can be attributed to: i) relatively large separation between the magnetically active ions (e.g., $r_{Co-Co} = 3.900$ Å) in the title compounds and ii) disorder in actual separation of the M-ions that occupy only half of the available M-sites.

The molar χ (T) dependence has been fitted with the Curie−Weiss law according to

$$\chi = \frac{N_A p^2 \mu_B^2}{3k_B(T - \Theta_W)} \quad (3)$$

where N_A is the Avogadro number, p is the effective magnetic moment in Bohr magnetons (μ_B), k_B is the Boltzmann constant,

dx.doi.org/10.1021/cm200117y |*Chem. Mater.* 2011, 23, 2586–2594

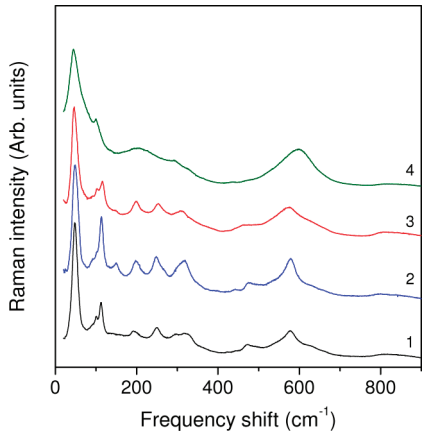

Figure 11. Room-temperature Stokes component of the Raman spectra of 1, $Ba_4MgTa_{10}O_{30}$; 2, $Ba_4CoTa_{10}O_{30}$; 3, $Ba_3ZnTa_8O_{24}$; and 4, $Ba_4CoNb_4Ta_6O_{30}$. Spectra are shifted along the Y-scale for clarity of presentation.

T is the absolute temperature, and Θ_W is the Weiss temperature. The results of the fit are listed in Table 7

Although the long-range magnetic ordering is not observed, the negative value of Θ_W and effective magnetic moments that are significantly lower that the free ion values indicate the possible existence of the short-range antiferromagnetic (AFM) interactions in the $Ba_4CoTa_{10}O_{30}$ and $Ba_4NiTa_{10}O_{30}$ compounds.

E. Raman Properties. Standard factor group analysis of the $Ba_4MTa_{10}O_{30}$ type compounds yields the zone center optical lattice vibrations for the *Cmmm* space group of $\Gamma = 10B_{1u} + 12B_{2u} + 13B_{3u} + 9A_g + 8B_{1g} + 6B_{2g} + 7B_{3g}$.

Among the 65 optical phonon modes, 35 are infrared active and 30 are Raman active. Room-temperature Raman spectra of several title compounds are shown in Figure 11. Among the 30 predicted Raman modes, 12 phonon modes are accounted for in the $Ba_4MgTa_{10}O_{30}$, $Ba_4CoTa_{10}O_{30}$ and $Ba_3ZnTa_8O_{24}$ compounds at room temperature. The missing modes could be either too weak or overlapping with the observed modes. The lowest energy mode which is also the most intense is located at around 48 cm^{-1}. Both $Ba_4MgTa_{10}O_{30}$ and $Ba_3ZnTa_8O_{24}$ compounds show qualitatively very similar Raman spectra which is another evidence of a similar crystal structure. Partial substitution of Nb for Ta (see, for example, $Ba_4CoNb_4Ta_6O_{30}$ spectrum in Figure 11) causes a red shift of the lowest energy phonon and, more importantly, a remarkable increase in the phonon damping coefficient as supported by the observed broadening in the Raman peaks. Large anharmonic component of the lattice vibrations in the Nb-doped samples is another evidence of the close proximity to the thermodynamic stability limit in the $Ba_4MTa_{10-x}Nb_xO_{30}$ phases.

4. CONCLUSIONS

Novel family of the incipient ferroelectrics based on the $Ba_4MNb_xTa_{10-x}O_{30}$ phases with *Cm* space group ground state has been reported here. Thermodynamic stability of these phases with respect to Nb dopant concentration was determined based on the XRD and EPMA analysis. Dielectric relaxation properties of the title compounds were characterized in the broad temperature (3−300 K) and frequency (100 Hz to 2 MHz) range. It was found that the dielectric properties show a typical incipient ferroelectric behavior with dielectric constant raising upon decrease in temperature. Substitution of Nb for Ta results in occurrence of the low-temperature dielectric anomaly similar to that observed in the relaxor-type ferroelectrics. Suitable values of the dielectric constant of these compounds ($\varepsilon' \approx 70-130$) makes them possible candidates for replacement of the rare-earth-based microwave dielectric resonators operating in the 1−2.5 GHz range provided that the tan δ and τ_ε values are properly optimized.

AUTHOR INFORMATION

Corresponding Author
*E-mail: kolodiazhnyi.taras@nims.go.jp.

ACKNOWLEDGMENT

This work was supported by Grant-in-Aid for Scientific Research C 21560025 from MEXT Japan provided to T.K. The authors are grateful to Kosuke Kosuda for the EPMA analysis.

REFERENCES

(1) Cruickshank, D. *J. Eur. Ceram. Soc.* **2003**, *23*, 2721.
(2) Aichele, T.; Lorenz, A.; Hergt, R.; Görnert, P. *Cryst. Res. Technol.* **2003**, *38*, 575.
(3) Adam, J. D.; Davis, L. E.; Dionne, G. F.; Schloemann, E. F.; Stitzer, S. N. *IEEE Trans. Microwaves. Theory Tech.* **2002**, *50*, 721.
(4) Ohsato, H. *J. Eur. Ceram. Soc.* **2001**, *21*, 2703.
(5) Ismailzade, I. G. *Sov. Phys.—Crystallogr.* **1963**, *8*, 274.
(6) Krainik, N. N.; Isupov, V. A.; Bryzhina, M. F.; Agranovskaya, A. I. *Sov. Phys.—Crystallogr.* **1964**, *9*, 281.
(7) Kryshtop, V. G.; Devlikanova, R. U.; Fesenko, E. G. *Inorg. Mater.* **1979**, *15*, 2257.
(8) Kryshtop, V. G.; Devlikanova, R. U.; Filip'ev, V. S.; Fesenko, E. G. *Inorg. Mater.* **1983**, *19*, 851.
(9) Nomura, S.; Toyama, K.; Kaneta, K. *Jpn. J. Appl. Phys.* **1982**, *21*, L624.
(10) Nomura, S. *Ferroelectrics* **1983**, *49*, 61.
(11) Kolodiazhnyi, T.; Belik, A. A.; Ozawa, T. C.; Takayama-Muromachi, E. *J. Mater. Chem.* **2009**, *19*, 8212 and references therein.
(12) Moussa, S. M.; Claridge, J. B.; Rosseinsky, M. J.; Clarke, S.; Ibberson, R. M.; Price, T.; Iddles, D. M.; Sinclair, D. C. *Appl. Phys. Lett.* **2003**, *82*, 4537.
(13) Mallinson, P. M.; Allix, M. M. B.; Claridge, J. B.; Ibberson, R. M.; Iddles, D. M.; Price, T.; Rosseinsky, M. J. *Angew. Chem., Int. Ed.* **2005**, *44*, 7733.
(14) Mallinson, P.; Claridge, J. B.; Iddles, D.; Price, T.; Ibberson, R. M.; Allix, M.; Rosseinsky, M. J. *Chem. Mater.* **2006**, *18*, 6227.
(15) Bieringer, M.; Moussa, S. M.; Noailles, L. D.; Burrows, A.; Kieley, C. J.; Rosseinsky, M. J.; Ibberson, R. M. *Chem. Mater.* **2003**, *15*, 586.
(16) Ikeda, T.; Haraguchi, T.; Onodera, Y.; Saito, T. *Jpn. J. Appl. Phys.* **1971**, *10*, 987 and references therein.
(17) Lufaso, M. W. *Chem. Mater.* **2004**, *16*, 2148.
(18) Jasper-Tönnies, B.; Müller-Buschbaum, H. *Monatsh. Chem.* **1984**, *115*, 1151.
(19) Brandt, R.; Müller-Buschbaum, H. *Z. Anorg. Allg. Chem.* **1986**, *542*, 18.
(20) Brandt, R.; Müller-Buschbaum, H. *Z. Anorg. Allg. Chem.* **1987**, *551*, 13.
(21) Vanderah, T. A.; Pickett, E.; Levin, I.; Roth, R. S. Ternary subsolidus for the system BaO−ZnO−Ta_2O_5. *AcerS-NIST Phase Equilibria*

Diagrams. NIST Standard Reference Database 31; National Institute of Standards and Technology: Gaithersburg, MD, 2005; Figure 11283.
(22) Kolodiazhnyi, T.; Fujita, K.; Wang, L.; Zong, Y.; Tanaka, K.; Sakka, Y.; Takayama-Muromachi, E. *Appl. Phys. Lett.* **2010**, *96*, 252901.
(23) *Bruker SMART-NT Version 5.625, SAINT-Plus Version 6.35A, SHELXTL Version 6.10*; Bruker AXS Inc.: Madison, WI, 2002.
(24) Kumada, N.; Kinomura, N. *J. Solid State Chem.* **1996**, *123*, 285.
(25) Barrett, J. H. *Phys. Rev.* **1952**, *86*, 118.
(26) Lemanov, V. V.; Sotnikov, A. V.; Smirnova, E. P.; Weihnacht, M.; Kunze, R. *Solid State Commun.* **1999**, *110*, 611.
(27) Lemanov, V. V.; Smirnova, E. P.; Tarakanov, E. A. *Phys. Solid State* **1997**, *39*, 628.
(28) Lemanov, V. V. *Phys. Solid State* **1997**, *39*, 1468.
(29) Samara, G. A.; Morosin, B. *Phys. Rev. B* **1973**, *8*, 1256.
(30) Samara, G. A.; Peercy, P. C. *Phys. Rev. B* **1973**, *7*, 1131.
(31) Samara, G. A. *J. Phys.: Condens. Matter* **2003**, *15*, R367 and refrences therein.
(32) Valant, M.; Kolodiazhnyi, T.; Axelsson, A.-K.; Gunda, S. B.; Alford, N. McN. *Chem. Mater.* **2010**, *22*, 1952.
(33) Höchli, U. T. *Phys. Rev. Lett.* **1982**, *48*, 1494.
(34) Valant, M.; Suvorov, D.; Rawn, C. J. *Jpn. J. Appl. Phys.* **1999**, *38*, 2820.